

Bare Demo of IEEEtran.cls for IEEE Computer Society Conferences

Isaac Sacramento
and Mauro Roisenberg
and Rodrigo Exterkoetter
*Department of Computer Science
Federal University of Santa Catarina
Florianopolis, Santa Catarina
Email: isaac.sacramento@posgrad.ufsc.br*

Leando P. de Figueiredo
*Department of Physics
Federal University of Santa Catarina
Florianopolis, Santa Catarina
Email: homer@thesimpsons.com*

Abstract—In this paper we will present a new convolution neural network model to deblurr post-inversion acoustic impedance images.

1. Introduction

Deblurring is the task of estimating a sharp latent image, given a blurry image as input. Recovering the original image is possible if the details of the blurring method are known, but in most cases, blurry images lack of enough information to recover a unique image. It is not observable in the literature an algorithm for deblurring all objects. Thus, methods that exploit domains-specific knowledge have emerged for deblurring categories of objects, e.g., text, faces and motion images. Similarly, the focus of this work is in post-inversion acoustic impedance deblurring. Obtaining high resolution acoustic impedance images, through seismic inversion methods, is a critical part in oil reservoir characterization. Despite the notorious efficiency of the inversion methods, post-inversion images deblurring has not received much attention.

Reservoir characterization aims to determine a multidimensional structure and properties of an oil field. To achieve this goal, it is essential to combine, through an inversion algorithm, the informations, knowledges and available data about the field, in such a way that it is possible to make the quantitative predictions about the reservoir behavior [8]. The seismic data is widely used in inversion processes because of its facility and precision in interpreting the acoustic impedance property. To succeed in seismic inversion, it is necessary to include strategies to deal with multiple sources of uncertainties. Specifically, the limited band-width of the seismic data leads to a misinterpretation of the resulting acoustic impedance models. According to [2], improving the resolution of seismic inversion is possible by adding high frequency in acquisition and processing seismic data. However, the earth attenuation, high-frequency noise and other sources, causes the lack of high and low frequencies in seismic data. Thus, deblurring the acoustic impedance

models, as a post-inversion refinement process, should lead to a more accurate interpretation of the impedance models.

Deblurring is generally modeled as the convolution of a blur kernel k with a latent image I :

$$y = k \otimes I + n \quad (1)$$

where n is the noise. Since k , I and n are unknown, the problem is highly ill-posed and admits infinity solutions for k and I . Several works have developed different deblurring methods for specific purposes. Blind deconvolution methods are widely investigated in image processing [25]. For the last six years, considerable effort has been employed in single image [17], [26], [33], [34] and multi-image [35], [36] blind deconvolutions. Applying blind deconvolution generally implies in making assumptions on blur kernels and/or on latent images. For example, assuming sparsity of blur kernel or that natural images have super-Gaussian statistics. The second assumption leads to the use of image priors on inference process and, consequently, to the maximum *a posteriori* (MAP) estimation [26]. However, [16] show that deblurring methods based on this prior tend to favor blurry images over original latent images.

The Bayesian inference approach [16] outperforms the MAP based methods. It marginalizes the image from the optimization step, while estimating the unknown blur. The authors show that it is possible to define a class of prior image based on natural image statistics, suitable enough for representing sharp images features. This prior formulation makes possible to use Bayesian inference in the estimation of the unknown image and the blur kernel. According to [27], defining a gradient prior, by itself, is not sufficient to reach a sharp image, instead, they search in a dataset for a prior that densely correspond to the blurry image similar to a sharp image. This search is an iteratively optimization over the correspondence between the images, the kernel and the sharp image estimation. Although [28] suggest a generalization for the method proposed by [27], it still requires a similar reference image, which is not always available.

The optimization methods previously described use a set of priors based on generic image statistics or domain-specific priors. It has been demonstrated that these methods work properly on synthetic blurs. However, newly studies show that they failure when applied to real world blurry images [29] and take a severe computational cost [30]. In contrast, the learning-based methods have gained attention with the resumption and recent advances in neural networks. The adequate hyper-parameter adjustment allows neural network to learn non-linear function or blur kernels. Thus, deblurring becomes a function of a blurry image I and a set of parameters p as

$$y = \sigma(I, p) \quad (2)$$

Learning-based methods focus on developing a model to learn the function σ [31] and to perform non-blind deblurring [30]. [32] learn a convolution neural networks (CNN) to recognize motion kernels and performs non-blind deconvolution in dense motion field estimate, in addition, [31] minimize regularized l_2 in order to perform text deblurring. We approach the acoustic impedance deblurring through a CNN model. CNN is a framework of deep learning which has been used in a wide sort of machine learning tasks. The availability of benchmarks [11] and the advances in Graphical Processing Unit (GPU) [3] allowed CNN to outperform state-of-the-art techniques in detection [12], [13], model-free tracking [14], classification [15]. With excellence in feature learning, CNN achieved notorious success in image and video classification [18], [20], action and speech recognition [19], [21]. Under the perspective of the reservoir characterization, CNN has been applied to lithofacies recognition [4] and calculation [5]. However, there is a lack of researches on improving the resolution of images resulting from inversion processes.

In this paper, we propose a new multilayer convolution network model to perform deblurring in post-inversion acoustic impedance. Each network layer maps higher level features originated in the previews layers through convolutional blur kernels. To perform this mapping, the kernels, also named weights, are adjusted by minimizing a loss function. The model enhances the resolution of acoustic impedance images, resulting in sharp images with increased high-frequency band-width and lower noise. In order to train the model, we blur a set of the synthetic acoustic impedance images to create a dictionary of images of high and low resolution. Then, the pairs of blur and latent images are normalized and presented to the network as input and target, respectively. The core concept of our architecture is the combination of the convolution layers with regression layers, thus the convolutional layers learn the spatial structures existing in different acoustic impedance images, while the regression layer proceed the prediction of the property values.

2. Theoretical foundations

Inversion theory is used in several areas to infer parameters values related to physical processes based on experi-

mental data. Inversion modeling refers to using the current measurements of observable physical parameters in order to infer the current model parameters (not observable). The inversion problem is described as (Eq. 3)

$$m = F^{-1}(d) \quad (3)$$

where, F is the investigated physical system, and relates a set of model parameters $m = (m_1, m_2, \dots, m_n) \in R^n$ estimated through the observed data $d \in R^s$. Geophysical methods frequently involve the solution and assessment of inversion problems. Studying these problems allow inferring physical properties distributions in the earth subsurface, using measured data. Among these data, the seismic data is mainly used in seismic inversion, which plays an important role in reservoir characterization. From a practical perspective, solving seismic inversion problems improves the exploration and management in oil industry, once the seismic data is highly correlated to petrophysical properties, e.g., density and porosity in subsurface.

The offshore seismic data is the main observable data used in seismic inversion. To perform seismic acquisition, one sends pulses through a controlled artificial source and captures the vertical component responses in function of time. The seismic data is a composition of the wave pulse used in the acquisition, named wavelet, and the characteristic of the interfaces between rock layers, on which the wavelet reflects. This rock layer characteristic is called reflectivity coefficient and it is calculated as

$$r(t) = \frac{z(t + \delta t) - z(t)}{z(t + \delta t) + z(t)}, \quad (4)$$

where, $z(t)$ is the acoustic impedance, in function of time t , defined as $z(t) = \rho(t)v(t)$, where $\rho(t)$ is the rock density and $v(t)$ the propagation velocity of acoustic wave. Therefore, the seismic data $d(t)$ is modeled as a discrete convolution operation $*$ of the wavelet s with the reflectivity coefficient r as

$$d(t) = s(\tau) * \sum_{j=1}^N r(t - t_j) \delta(t - t_j) + e_d(t) \quad (5)$$

where, N is the number of subsurface layers, $e_d(t)$ is a random noise in function of time. One ideal wavelet is a delta pulse with all the frequency band-width, however, in practice wavelets have their band-width generally limited from $6Hz$ to $65Hz$. By consequence, the images resulting from the seismic inversion will keep their frequency spectrum limited.

According to [7], a good acoustic impedance model contains more information than the seismic data, because the inversion process contains additional information originated from well-logs, for exemple, a low-frequency model. The well-logs are real data measured in wells spread along the field. With the local acoustic impedance it is possible to calculate the low-frequency model by interpolation between wells [37], [38]. Despite of the low-frequency model, the final model for acoustic impedance still lacks of high resolution details.

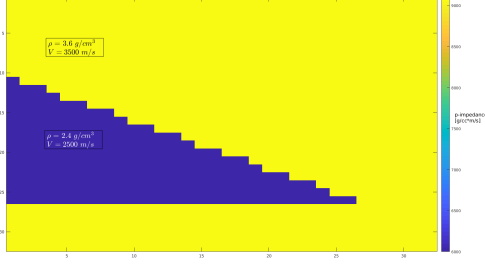


Figure 1. Wedge with reference values for density and compressional velocity.

3. Data and Methods

3.1. Acoustic Impedance Inversion

The experiments described in this paper were performed on a set of synthetic acoustic impedance images. Using synthetic models to test and parametrize algorithms is a common practice in reservoir characterization [10]. It allows studying the results of the algorithms without external interferences and performing efficient interpretations and assessments. According to [22], wedge shaped models is a straight way to analysis the seismic model and inversion processes. It reproduces reservoir contexts such as stratigraphic refinements, edges and channel structures in a realistic manner.

The training set generation is performed in two steps. The first step creates a set of wedge shapes represented by images with size 32 x 32. The wedges represent the reservoir and they randomly vary in width and length. The second step fills the lithology with values of petrophysical properties. In order to simplify the assessments and conclusions, the lithology structures are filled with constant reference values of rock densities and compressional velocity observed in the literature [39]. The acoustic impedance is calculated using the density and velocity models and the images in high resolution model are obtained, as illustrated in Fig. 1. In a real scenario, the blurry acoustic impedance is the result of an acoustic inversion method, such as Maximum *a posteriori* [37], [38], Sparse Spike [40] and Recursive Inversion [41], using seismic data with limited band-width. However, for experimental purpose, the acoustic impedance models were filtered and the high frequencies were removed to obtain the blurry images, as illustrated in Fig. 2. This way, the supervised learning is performed with the high resolution images and blurred images. To increase the number of examples in the training dataset we rotate the impedance models in angles integer multiples of right angle. This approach allows the model learning the maximum edge variabilities in wedges images.

3.2. Convolutional Neural Network

The workflow of the proposed method consists of the following steps:

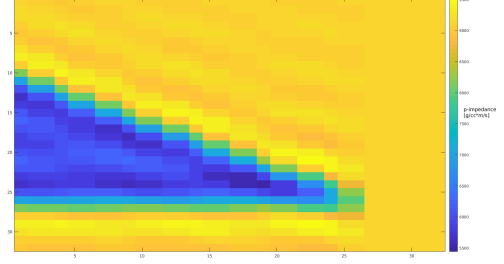


Figure 2. Acoustic impedance blurred model.

- Generate the synthetic impedance images;
- Blur the images through a low-pass filter;
- Train the convolutional model with the pair of high and low resolution images;
- Test the model with different blurry images;
- Assess the result for the testing output.

The CNN is a well established method for pattern recognition and image classification. Thus, an important breakthrough when applying CNN to deal with physical property images is developing a model capable to solve regression tasks. The model presented in this paper is able to solve two important problems related to deblurring physical properties images: (1) learning the spacial patterns in the low resolution training images and (2) predicting each pixel intensity value in the new higher resolution image. To reach these two goals, the model architecture consists of two convolution layers, each one followed by one pooling layer and a regularization layer. The second regularization layer is followed by a fully connected layer, which maps the convolution layer's output to 1024 neurons. The output model comprises a regression layer to predict the intensity value of each pixel.

The model performs a supervised learning through a dictionary containing pairs of low and high resolution images. The optimization algorithm adjusts the network weights in every layer by minimizing the Mean Squared Error (MSE) in each batch of images. Thus, after the training phase, the model is capable to deblur any other wedge shaped acoustic impedance image not presented in the training dataset. The outputted image recovers the high frequencies and presents higher similarity to the high resolution image than to the blurred image, according to a established metric. The model was adjusted to deblur a wide variety of wedge shapes and impedance values. Those wedges which the model was unable to predict were added in the training set.

Three metrics assess the performance of the convolution networks: Fast Fourier Transform Index - FFTI (Eq. 6), Rooted Mean Square Error - RMSE (Eq. 7). The FFTI is a similarity metric calculated based on the fast fourier transform (FFT) of each image. It is introduced by [23] and calculates as

$$C = \frac{(\sum_{i=1}^N F_{1i} F_{2i} - N \bar{F}_1 \bar{F}_2)^2}{(\sum_{i=1}^N |F_{1i}|^2 - N \bar{F}_1^2)(\sum_{i=1}^N |F_{2i}|^2 - N \bar{F}_2^2)}, \quad (6)$$

where, for each frequency, an intensity value is calculated from the real and complex parts of the fourier transform. F_{1i} represents the intensity value of i -th *pixel* in the first image and F_{2i} is the intensity value of i -th *pixel* in the second image. \bar{F}_1 e \bar{F}_2 are the mean frequencies in each image. The closer FFTI is to 1, the higher the similarity between the images. The frequencies spectrum is additionally useful to present the graphic of frequency magnitudes in the images. The frequency magnitude graphic allows distinguishing what high frequencies were added to the acoustic impedance after the low resolution image is passed through the trained CNN.

$$RMSE = \sqrt{\frac{(\sum_{i=1}^N (x_i - y_i)^2)}{N}}, \quad (7)$$

4. Experiments

To build the training dataset we generated 500 images of random wedge. Because the last layer of the network is a regression unit, it is necessary the normalization of the images to values between 0 and 1, and the results are presented in terms of this normalization. The normalized images are then rotated in four integer angles multiple of 90 degrees, then comprising a total of 2000 images. By doing so, we present to the network the same lithologies in different positions and expect that the network identify general sorts of wedges in angles different from those with which the it was trained. The rotated images are blurred by applying a low-pass filter with cutting frequency $4Hz$, then the pairs of blurred and not-blurred images are used to adjust the model weights. It is relevant to mention that the images which are blurred with the same cutting frequency and that remains simmetric after the rotation, have the values for the metrics MSE and FFTI. This means that rotating the images causes no changes in impedance values. We apply the same approach to generate different scenarios for test cases.

4.1. Implementation Details

The model is implemented using the Deep Learning toolbox delivered in MATLAB R2017A. For training the network, we used a mini-batch with size of 32 training examples. The network weights are randomly initialized and the Stochastic Gradient Descendant with Momentum (SGDM) [24] is the optimization algorithm. We adopted an exponentially decreasing learning rate (initially set to 0.005), decreasing every iteration in a total of 100 iterations. It should be noted that, once the wedge shapes are randomly generated, every image is different and each one is introduced only once to the network, this way avoiding overfitting. In the following subsection we present the results divided into those test cases in which the wedges are rotated in angles integer multiple of right angle and those in which the wedges are rotated according to a random angle.

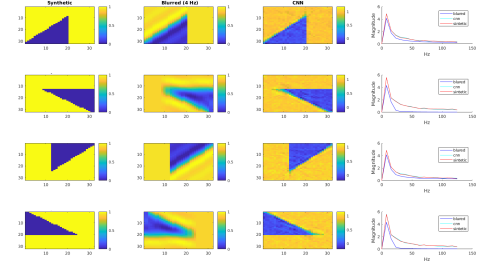


Figure 3. Acoustic impedance blurred model.

TABLE 1. AN EXAMPLE OF A TABLE

	Blurry Image	CNN Output
Example 1	0.1294	0.0644
	0.9819	0.9857
Example 2	0.1948	0.0774
	0.9549	0.9862
Example 3	0.1294	0.0645
	0.9819	0.9876
Example 4	0.1948	0.0775
	0.9575	0.9902

4.2. Integer Angles Rotated Wedges

In the first scenario, both the training and test images had the same reference values for density and compressional velocity. We also applied the same rotation to both set of images. The wedges in the testing set differ from the ones in the training set only by their shapes. Thus, the first experiment concerns to correctly modeling the shape of the wedges in the testing image and deblurr the edges and contours in a simple perspective. Fig. 3 presents the result obtained with the initial model applied to the test images. The first column shows the high resolution images, followed by the blurry images, the third column shows the result of the convolutional deblurring network and the fourth column shows the graph of frequency magnitudes of each image (synthetic, blurred and CNN). Table 1 presents the values for each metric obtained for the CNN output and the blurry image related to the latent image.

In the second scenario, we inverted the impedance values of the lithology structures. This way we verified that the prediction of the pixel value is disconnected to the lithology shape. Fig. 4 shows the results obtained in this scenario.

In the third scenario, we arbitrarily changed the normalized impedance to values of higher impedance out of the wedge (with value of 0.7) and lower impedance (with value of 0.3) into the wedge. These values are out the range learned by the model during the training phase. Doing this, we tested the model generalization capacity to reach the learned pixel intensity values. We observed that, once the model is trained with pixel valued to 0 and 1, the network poorly extrapolated and a new training dataset is generated

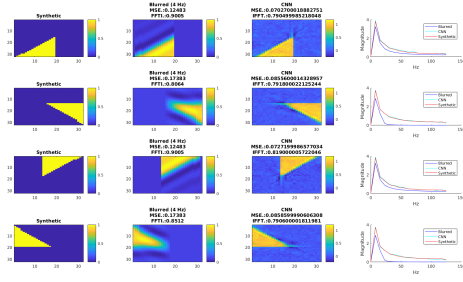


Figure 4. Acoustic impedance blurred with inverted property values.

TABLE 2. AN EXAMPLE OF A TABLE

	Blurry Image	CNN Output
Example 1	0.1248	0.0702
	0.9005	0.7904
Example 2	0.1738	0.0855
	0.8064	0.7918
Example 3	0.1248	0.0727
	0.9005	0.8190
Example 4	0.1738	0.0858
	0.8512	0.7906

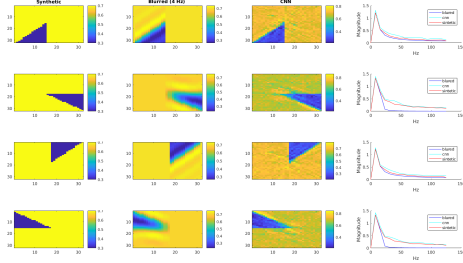


Figure 5. Acoustic impedance normalized to arbitrary values.

TABLE 3. AN EXAMPLE OF A TABLE

	Blurry Image	CNN Output
Example 1	0.3529	0.0333
	0.9901	0.9915
Example 2	0.0561	0.0444
	0.9744	0.9868
Example 3	0.3529	0.0319
	0.9901	0.9908
Example 4	0.0561	0.0435
	0.9746	0.9860

containing wedges with the new pixel values. The Fig. 5 shows the result for the network trained with the extended dataset.

A new scenario is simulated in which the synthetic images are blurred with different cutting frequencies. Each one

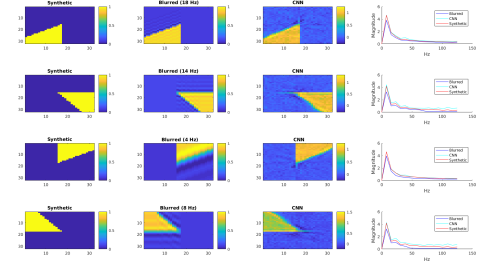


Figure 6. Acoustic impedance blurred with different frequencies.

TABLE 4. AN EXAMPLE OF A TABLE

	Blurry Image	CNN Output
Example 1 (18 Hz)	0.0933	0.0841
	0.9576	0.8094
Example 2 (14 Hz)	0.1277	0.0983
	0.9169	0.8001
Example 3 (4 Hz)	0.1228	0.0795
	0.9228	0.8299
Example 4 (8 Hz)	0.8946	0.7983
	0.0933	0.0841

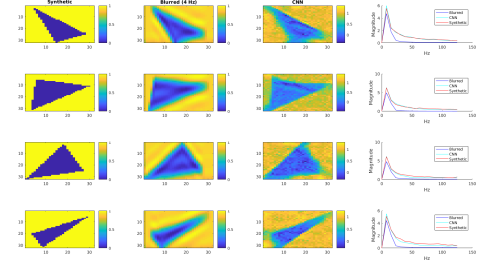


Figure 7. Acoustic impedance blurred model.

of the four test images are blurred with different frequency randomly chosen between 3 and 20 Hz. This is particularly interesting, because in a scenario with real data, physical aspects as signal attenuation may lead to different blurring profiles in post-inversion images. Fig. 6 shows the results for this scenarios.

4.3. Randomly Rotated Wedges

Randomly rotated wedge is related to a lithology positioned in a random angle. In this case, we evaluated the CNN capability to deblurr the lithologies with shape and position absent in the training dataset. Fig. 7 shows the test case in which the acoustic impedance is normalized to values 0 and 1. As the same range of values were used during the network training, it was able to predict the pixel intensity value.

TABLE 5. TABLE OF METRIC VALUES FOR WEDGES IN RANDOM POSITIONS AND ACOUSTIC IMPEDANCE NORMALIZED TO 0 AND 1.

	Blurry Image	CNN Output
Example 1	0.2155	0.2164
	0.9357	0.9361
Example 2	0.2248	0.2045
	0.9357	0.9235
Example 3	0.2197	0.2209
	0.9406	0.9236
Example 4	0.2174	0.1879
	0.9555	0.9549

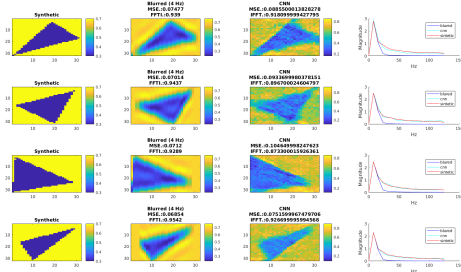


Figure 8. Acoustic impedance blurred model.

TABLE 6. TABLE OF METRIC VALUES FOR WEDGES IN RANDOM POSITIONS AND ACOUSTIC IMPEDANCE NORMALIZED TO 0.3 AND 0.7.

	Blurry Image	CNN Output
Example 1	0.0747	0.0885
	0.9390	0.9180
Example 2	0.07014	0.0933
	0.9437	0.8967
Example 3	0.0712	0.1046
	0.9289	0.8733
Example 4	0.0685	0.0751
	0.9542	0.9266

if using array.sty, it might be a good idea to tweak the value of as needed to properly center the text within the cells

TABLE 7. AN EXAMPLE OF A TABLE

One	Two
Three	Four

Table 5 presents the metric values for the test examples in which the wedges are randomly positioned.

In this same scenario, we normalized the values of impedance to range equal to 0.3 and 0.7, as illustrated in Fig. 8. These values were absent in the training dataset and it is notable a wider spread of values in both lithologies outputted by the network.

Tab. 6 presents the values error values for this test case. It is notable that.

5. Conclusion

The conclusion goes here.

Acknowledgments

The authors would like to thank...

References

- [1] H. Kopka and P. W. Daly, *A Guide to L^AT_EX*, 3rd ed. Harlow, England: Addison-Wesley, 1999.
- [2] Xi Xiaoyu, Ling Yun, Sun Desheng, Guo Xiangyu, and Wang Huifeng, "Studying the effect of expanding low or high frequency on post-stack seismic inversion," in SEG Technical Program Expanded Abstracts 2012. September 2012, 1-5.
- [3] Buduma, N., "Fundamentals of Deep Learning," Academic Press, 2015, in O'Reilly Media.
- [4] Qian Feng, Yin Miao, Su Ming-Jun, Wang Yaojun, Hu Guangmin, "Seismic facies recognition based on prestack data using deep convolutional autoencoder,"
- [5] Liu Lihui, Lu Rong, Li Jianhai, Yang Wenkui, "Seismic Lithofacies Computation Method Based on Deep Learning," p. 649-652.
- [6] G. G. Chrysos, S. Zafeiriou, "Deep Face Deblurring," 2017 IEEE Conference on Computer Vision and Pattern Recognition Workshops (CVPRW), Honolulu, HI, 2017, pp. 2015-2024.
- [7] Rebecca Buxton Latimer, Rick Davidson, Paul van Riel, "An interpreter's guide to understanding and working with seismic-derived acoustic impedance data," 2017, pp. 242-256, v. 19, num. 3, in The Leading Edge.
- [8] JJM. Buiting, M. Bacon, "Using geophysical, geological, and petrophysical data to characterize reservoirs in the North Sea," in 5th Conference on Petroleum Geology of NW Europe, London. CD-ROM.
- [9] Paul van Riel, "The past, present and future of quantitative reservoir characterization," in The Leading Edge, 19, p. 878881.
- [10] Sergio Sacani Sancevero, Armando Zaupa Remacre, Rodrigo de Souza Portugal, "O papel da inverso para a impedncia no processo de caracterizao ssmica de reservatrios," in Revista Brasileira de Geofisica, 2006, p. 495-512, v. 24.
- [11] O. Russakovsky, J. Deng, H. Su, J. Krause, S. Satheesh, S. Ma, Z. Huang, A. Karpathy, A. Khosla, M. Bernstein, "Imagenet large scale visual recognition challenge," in International Journal of Computer Vision (IJCV), p. 211252, 2015.
- [12] R. Girshick, "Fast r-cnn," In IEEE Proceedings of International Conference on Computer Vision (ICCV), pages 14401448, 2015.
- [13] S. Bell, C. L. Zitnick, K. Bala, and R. Girshick, "Inside-outside net: Detecting objects in context with skip pooling and recurrent neural networks," in arXiv preprint arXiv:1512.04143, 2015.s
- [14] H. Nam and B. Han, "Learning multi-domain convolutional neural networks for visual tracking," In IEEE Proceedings of International Conference on Computer Vision and Pattern Recognition (CVPR). IEEE, 2016.
- [15] K. He, X. Zhang, S. Ren, and J. Sun, "Deep residual learning for image recognition," In IEEE Proceedings of International Conference on Computer Vision and Pattern Recognition (CVPR). IEEE, 2016.
- [16] A. Levin, Y. Weiss, F. Durand, and W. T. Freeman. "Understanding and evaluating blind deconvolution algorithms." In IEEE Proceedings of International Conference on Computer Vision and Pattern Recognition (CVPR), p. 19641971.
- [17] A. Levin, Y. Weiss, F. Durand, and W. T. Freeman. "Efficient marginal likelihood optimization in blind deconvolution." In CVPR, 2011.

- [18] A. Krizhevsky, I. Sutskever, G. E. Hinton, "Imagenet classification with deep convolutional neural networks: Advances in neural information processing systems," 2012, p. 10971105.
- [19] S. Ji, W. Xu, M. Yang, K. Yu, 2013, "3d convolutional neural networks for human action recognition," in IEEE transactions on pattern analysis and machine intelligence, n. 35, p. 221231.
- [20] O. Abdel-Hamid, A.-r. Mohamed, H. Jiang, L. Deng, G. Penn, D. Yu, 2014, "Convolutional neural networks for speech recognition," in IEEE/ACM Transactions on audio, speech, and language processing, n. 22, p. 15331545.
- [21] S. S. Farfate, M. J. Saberian, L.-J. Li, 2015, "Multi-view face detection using deep convolutional neural networks," in Proceedings of the 5th ACM on International Conference on Multimedia Retrieval, ACM, p. 643650.
- [22] P. J. Harvey, D. J. MacDONALD, "Seismic modelling of porosity within the jurassic aged carbonate bank, offshore Nova Scotia," in Canadian Journal of Exploration Geophysics, n. 26, p. 5471.
- [23] S. Narayana, P. K. Thirivikraman, "Image similarity using fourier transform," in International Journal of Computer Engineering and Technology, 2015, n. 6, p. 2937.
- [24] N. Qian, "On the momentum term in gradient descent learning algorithms," in Neural Networks, v. 12, i. 1, 1999, p. 145-151.
- [25] T.E. Bishop, S.D. Babacan, Amizic, T. Chan, R. Molina, A. Katsaggelos, "Blind image deconvolution: problem formulation and existing approaches," in. Blindimage deconvolution: theory and applications, CRC press (2007).
- [26] S. D. Babacan, R. Molina, M. N. Do, and A. K. Katsaggelos, "Bayesian blind deconvolution with general sparse image priors." In. Proceedings of European Conference on Computer Vision (ECCV), p. 341355, 2012.
- [27] Y. Hachohen, E. Shechtman, and D. Lischinski, "Deblurring by example using dense correspondence." In IEEE Proceedings of International Conference on Computer Vision (ICCV), p. 23842391, 2013.
- [28] J. Pan, Z. Hu, Z. Su, M. H. Yang., "Deblurring face images with exemplars." In Proceedings of European Conference on Computer Vision (ECCV), p. 4762. Springer, 2014.
- [29] W.S. Lai, J. B. Huang, Z. Hu, N. Ahuja, M. H. Yang, "A comparative study for single image blind deblurring." In IEEE Proceedings of International Conference on Computer Vision and Pattern Recognition (CVPR). IEEE, 2016.
- [30] A. Chakrabarti. "A neural approach to blind motion deblurring." In Proceedings of European Conference on Computer Vision (ECCV), p. 221235. Springer, 2016.
- [31] M. Hradis, J. Kotera, P. Zemck, F. Sroubek. "Convolutional neural networks for direct text deblurring." In Proceedings of British Machine Vision Conference (BMVC), 2015.
- [32] J. Sun, W. Cao, Z. Xu, J. Ponce. "Learning a convolutional neural network for non-uniform motion blur removal." In IEEE Proceedings of International Conference on Computer Vision and Pattern Recognition (CVPR), p. 769777, 2015.
- [33] D. Krishnan, T. Tay, R. Fergus. "Blind deconvolution using anormalized sparsity measure." In CVPR, 2011.
- [34] H. Zhang, J. Yang, Y. Zhang, N. M. Nasrabadi, T. S. Huang. "Close the loop: Joint blind image restoration and recognition with sparse representation prior." In ICCV, 2011.
- [35] F. Sroubek and P. Milanfar. "Robust multichannel blind deconvolution via fast alternating minimization." in IEEE Trans. on Image Processing, p. 16871700, 2012.
- [36] X. Zhu, F. Sroubek, P. Milanfar. "Deconvolving PSFs for a better motion deblurring using multiple images." In ECCV, 2012.
- [37] L. P. Figueiredo, M. Santos, M. Roisenberg, G. Neto, W. Figueiredo, "Bayesian framework to wavelet estimation and linearized acoustic inversion," In Geoscience and Remote Sensing Letters, 2012, p. 15.
- [38] A. Buland, H. Omre, "Bayesian linearized avo inversion," In Geophysics, 2003, p. 185198.
- [39] G. Mavko, T. Mukerji, J. Dvorkin, "The Rock Physics Handbook: Tools for Seismic Analysis of Porous Media." 2009 Cambridge: Cambridge University Press, p. 359-369.
- [40] H. DEBEYE, P. RIEL van, "Lp-norm deconvolution." 1990, Geophysical Prospecting, p. 381403
- [41] S. Chopra, "Integrating coherence cube imaging and seismic inversion." 2001, The Leading Edge, p. 354362.